ELSEVIER

Materials Science and Engineering A272 (1999) 152–162

MATERIALS SCIENCE & ENGINEERING A

www.elsevier.com/locate/msea

Dislocation dynamics in the oxide dispersion strengthened alloy INCOLOY MA956☆

M. Bartsch [a], A. Wasilkowska [b], A. Czyrska-Filemonowicz [b], U. Messerschmidt [a,*]

[a] *Max Planck Institute of Microstructure Physics, Weinberg 2, D-06120 Halle/Saale, Germany*
[b] *Faculty of Metallurgy and Materials Science, University of Mining and Metallurgy, Al. Mickiewicza 30, Krakow 30-059, Poland*

Abstract

In situ straining experiments in a high-voltage electron microscope have been performed on the oxide dispersion strengthened alloy INCOLOY MA 956 at room temperature and between 640 and 1010°C to study the dynamic behaviour of dislocations. Macroscopic compression experiments including stress relaxation tests have been carried out between room temperature and 900°C. The dynamic behaviour of dislocations, the flow stress and its strain rate sensitivity are discussed in the different temperature ranges in terms of long-range dislocation interactions, the Orowan mechanism, the model of the thermally activated detachment of dislocations from oxide particles, solution hardening and a diffusional point defect drag. It is concluded that the latter controls the thermally activated dislocation processes in a wide temperature range around about 700°C. The detachment model may be active only above 900°C. © 1999 Elsevier Science S.A. All rights reserved.

Keywords: Dislocations; Ferritic steel; In situ straining experiments in HVEM; Orowan stress; Oxide dispersion strengthening; Strain rate sensitivity

1. Introduction

Hard incoherent particles can be incorporated into a metal matrix in order to improve the creep resistance of alloys at high temperatures. Frequently, the particles are oxides leading to oxide dispersion strengthened (ODS) alloys. At low temperatures, such particles have to be bypassed by Orowan looping. At high temperatures, the dispersoids are easily overcome by climb [1]. Nevertheless, there exists a well-defined threshold stress for creep, below which the ODS alloys exhibit very low creep rates. The interpretation of the threshold stress is based on an attractive interaction which causes a pinning of the moving dislocations at the departure side of the particles [2]. It was stated that if the interfaces between the particles and the matrix do not transfer shear strains, the stress field of the dislocations may partly relax at the interface leading to a reduced dislocation energy [3,4], which causes the attractive interaction. Most experimental data on the creep behaviour of ODS alloys are interpreted in terms of the respective model [5] or its variant, including the thermally activated detachment from the particles [6]. There is some transmission electron microscopic evidence of dislocations pinned to particles (e.g. Refs. [7,8]) but there is no direct proof that the dislocations spend most of their time in the respective configurations at the departure side of the particles. In situ straining experiments in a transmission electron microscope should be a suitable means to study the dislocation dynamics and the interaction between dislocations and particles in ODS alloys. However, since the interparticle distance of the order of magnitude of 100–150 nm is in the range of the specimen thickness in conventional transmission electron microscopes, a high-voltage electron microscope (HVEM) should be used, which allows thicker foils to be transmitted. Such studies have not been reported previously, except one experiment showing the

☆ This paper is dedicated to Professor Herbert Herman on the occasion of his 65th birthday.

* Corresponding author. Tel.: +49-345-5582927; fax: +49-345-5511223.

E-mail address: um@mpi-halle.mpg.de (U. Messerschmidt)

PII: S0921-5093(99)00471-2

interaction between superdislocations and a single particle [9].

The present paper reports on an HVEM in situ deformation study on the ferritic ODS alloy INCOLOY MA956. The microstructure and the deformation properties of this oxidation-resistant material are described in Refs. [8,10,11]. First results of the present experiments were published in Ref. [12]. The in situ experiments are supplemented by two macroscopic deformation tests to analyse the strain rate sensitivity of the flow stress.

2. Experimental

The studied alloy INCOLOY MA956 consists (in wt%) of Fe–19.9Cr–4.6Al–0.38Ti–0.51Y–0.019C–0.014N–0.19O. Microtensile samples of $8 \times 2 \times 0.1$ mm^3 in size for in situ straining experiments were prepared from large grains with a unique orientation of the alloy. The samples were dimpled before the two-step electrolytic jet polishing between platinum masks. The experiments were performed in an HVEM operated at 1000 kV using double tilting straining stages either for room temperature [13] or for high temperatures [14]. All functions of the stages are controlled by a personal computer. Five successful experiments were carried out, one at room temperature and the others around 700°C, where the temperature was changed afterwards including temperatures of 640, 660, 790, 880, 970 and 1010°C. The specimens were loaded in small load increments. The dislocation configurations were recorded photographically or by a video system.

Two macroscopic compression tests were carried out in order to obtain data on the temperature and strain rate sensitivity of the flow stress. The respective specimens of $1.25 \times 1.5 \times 4.3$ mm^3 in size were cut from a single grain so that they had equal orientation. Each specimen was tested at different temperatures. The strain rate sensitivity $r = \Delta\sigma/\Delta \ln \dot{\varepsilon}$ was measured by stress relaxation tests, where r equals the reciprocal slope in a plot of the logarithm of the negative relaxation rate versus the stress, i.e. $r = \Delta\sigma/\Delta \ln(-\dot{\sigma})$, where σ is the (normal) stress and $\dot{\varepsilon}$ is the strain rate. A few strain rate cycling tests were performed to confirm the results of the stress relaxation tests.

3. Results

3.1. Slip systems

The activated slip planes were determined from the traces the moving dislocations generated at the specimen surfaces. Starting from the diffraction diagram of the pole near which the dislocation structures were recorded, the orientation and width of possible slip traces were calculated by a computer program allowing also for deviations of the foil normal from the orientation of the pole. In most of the cases, the slip planes could be identified clearly. Hence, at room temperature the dislocations moved on {110} planes, at high temperatures also on {112} and {123} planes. The directions of possible Burgers vectors of $1/2\langle 111\rangle$ type were concluded from the orientation factor and from the shape of the bowed-out segments (see Section 3.3). Calculated shapes of dislocation loops bowing out under stress are included in Figs. 1–3 at an enlarged size in the projection on the respective image planes.

3.2. Dynamic behaviour of dislocations

As described above, at room temperature slip was observed only on {110} planes. At the beginning of the in situ experiments, slip mainly occurs in relatively narrow slip bands, as shown in Fig. 1. The slip plane is inclined to the image plane by about 65° so that the dislocations appear only in a narrow projection. Resting dislocations mainly have screw character, being quite straight then. Only edge or mixed segments bow out strongly. The dislocations move in a jerky way over distances longer than those between the oxide particles. With increasing strain, the dislocations cross slip onto another {110} plane leading to a broadening of the slip bands until the whole volume is filled with dislocations.

At elevated temperatures, slip occurs on {110}, {112} and {123} planes often including cross slip between these planes. Most experiments were made at 700°C. At this temperature, the dislocations stop at obstacles but move smoothly between them. The mode of motion depends somehow on the inclination of the slip planes with respect to the foil plane, leading to different slip plane widths. An example of a dislocation on a steeply inclined plane is given in Fig. 2. In Fig. 2a, the dislocation marked by arrows bows out weakly between obstacles. When the left part slowly moves forward, a very deep cusp is formed in Fig. 2b, suggesting that the dislocation is pinned to a large particle. Strong bowings appear also in Fig. 2d, e. The active obstacles are usually not visible before they pin the dislocations. The distances between stable positions amount to about 300 nm. The dislocation moves smoothly and continuously between the pinned configurations.

As the motion of dislocations on the steeply inclined slip planes is obviously influenced by the small width of these planes, mostly containing only two bowed-out segments, the video sequence shown in Fig. 3 was chosen for further evaluations with a slip plane tilted by only about 25° with respect to the image plane. In this configuration, the width of the slip plane was about 1 μm. The average dislocation velocity was 10–15 nm s^{-1}, which is slow enough to resolve different stages of

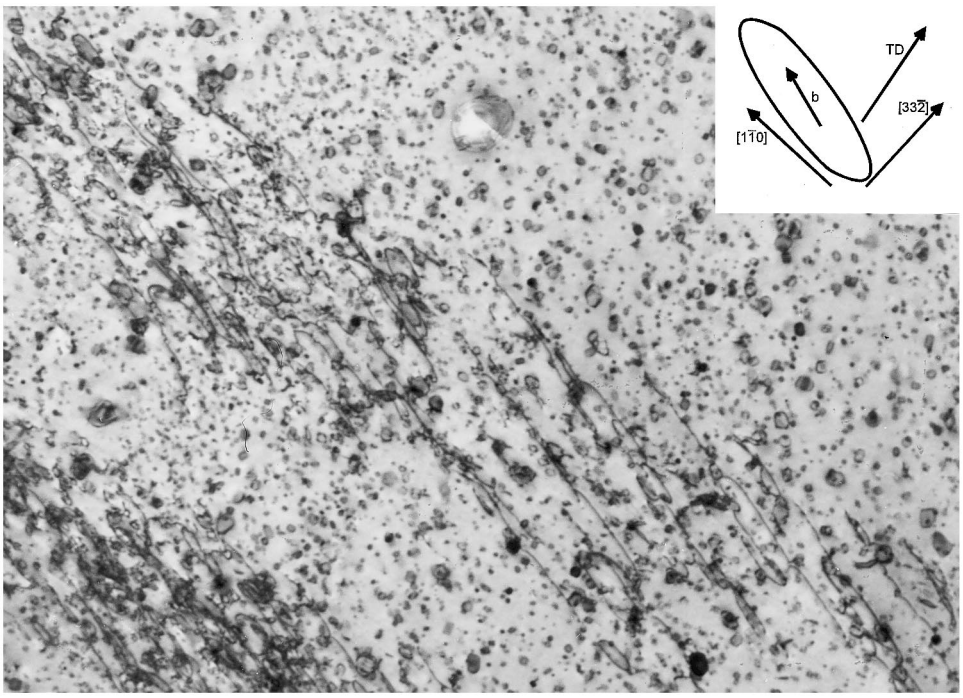

Fig. 1. Dislocations moving on {011} slip planes during in situ deformation of the alloy INCOLOY MA956 in an HVEM at room temperature. The [1$\bar{1}$1] direction corresponds to the direction of the traces of the slip planes. The calculated equilibrium shape of dislocations with Burgers vector b is presented in the projection of their slip plane onto the image plane of the electron micrograph. TD is the tensile direction. It is similar in Figs. 2–4.

overcoming the dispersoids. The dislocation velocity was approximately equal for screw and edge dislocations. The first part of this sequence shows several stages of surmounting a single strong obstacle. In the first video frame taken at a time of 0 s the obstacle is first contacted. Afterwards, the dislocation moves from the arrival side to the departure side of the obstacle in about 7 s forming only a weak cusp at the obstacle. It then slowly bows out reaching its equilibrium bowing after a total time of 21 s. In this configuration, the dislocation forms a sharp cusp at the departure side of the obstacle. It remains in this position for less than 1 s. At 21.6 s, the dislocation starts to detach from the obstacle. At 22.7 s, it has left the particle completely, the strong bowing has disappeared and the dislocation moves in a viscous way. While travelling to the next particle, which takes about 10 s, most of the dislocation is quite straight. Certainly, the particle that had been overcome during the first 22 s was a particularly large one. Nevertheless, the process is very much the same also for smaller particles, which are not imaged in the HVEM but which cause the formation of cusps along the dislocation line, as described before in connection with Fig. 2.

As Figs. 2 and 3 show, around 700°C the four following stages of dislocation motion in an array of incoherent particles can be distinguished.

1. The dislocations move in a viscous way between configurations in which they are locally pinned. This points to a frictional force acting on the moving dislocations.
2. After contacting a particle, the dislocation overcomes it in rather a short time, with a relatively small force acting.
3. The dislocation gets pinned at the departure side of the particle while the adjacent segments in the matrix slowly bow out until reaching their elastic equilibrium configurations. This process of bowing out between the particles takes a relatively long time. The back stress of the bowed segments reduces the stress available for the viscous motion, causing a lower velocity before the equilibrium bowing is reached. The back stress, which reduces the applied stress temporarily, is supposed to be the main strengthening effect of the particles around 700°C.
4. After a short lifetime of the equilibrium configuration, the dislocation detaches from the particle, straightens and glides to the next obstacle as described under (1).

Fig. 4 presents dislocation configurations during the deformation of a single specimen at different temperatures. All configurations resemble those at 700°C. However, while the dislocation motion at 660°C is viscous between the stable configurations and the slip distances after overcoming the particles are not much larger than the particle distances, the motion becomes jerky at higher temperatures with high velocities between the particles, suggesting that the frictional forces, which act

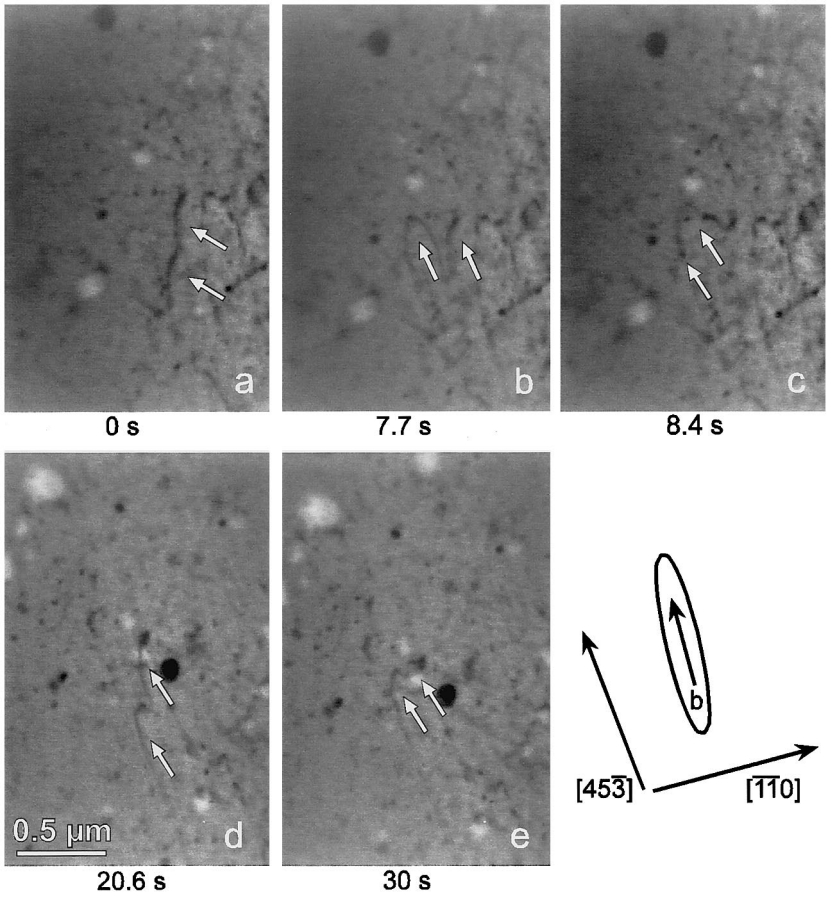

Fig. 2. Video sequence of a dislocation moving at 700°C on a {112} plane inclined by about 60° with respect to the image plane.

at temperatures around 700°C, disappear at higher temperatures. In addition, the slip distances become larger than a micrometer. At 1010°C, the dislocations mostly move in a collective way.

3.3. Quantitative description of dislocation configurations and motion

The density of effective obstacles on the slip plane is represented by the distance l between the centres of obstacles along the dislocation line. The sites of obstacles along the dislocation are marked by cusps in the dislocation limiting the bowed-out segments so that l can be measured as the distance between these cusps. As shown in Fig. 1, at room temperature most dislocations imaged are quite straight screw dislocations. Owing to the low curvature and the superposition of the contrast of the dislocations on that of the particles, the cusps in the dislocations are not clearly revealed. Accordingly, the obstacle distance l has not been determined for room temperature. A value of $l = 141$ nm is observed on strongly bowed-out segments. It will be used below for determining the effective stress but it does not represent the average length of all dislocation segments.

Some efforts were made to measure l at 700°C. First, the distances were determined between the cusps in all bowed-out positions, which were recorded during a 3-min observation of the dynamic video sequence, a section of which is given in Fig. 3. Fig. 5 shows a histogram of the measured distances, the average value of which is $l = 220$ nm. No data were obtained below about 75 nm owing to the limited spatial resolution of the video records. In a second approach, video frames were selected randomly for determining the pinning point distances of a larger number of segments. The average value was about 190 nm. For strong obstacles, l should be equal to the square root of the area swept per obstacle. In the video sequence presented in Fig. 3, the average area swept by the moving dislocation was about 0.05 μm^2 per obstacle, yielding again $l \cong 220$ nm. As can be concluded from these three measurements, the segment length l between such obstacles which effectively impede the dislocation motion at about 700°C amounts to about 200 nm.

The stress acting on individual bowed-out dislocation segments was determined from the dislocation curvature. To this end, the shape of bowed-out segments under a shear stress τ was compared with that calculated using the line tension approach in an elastically

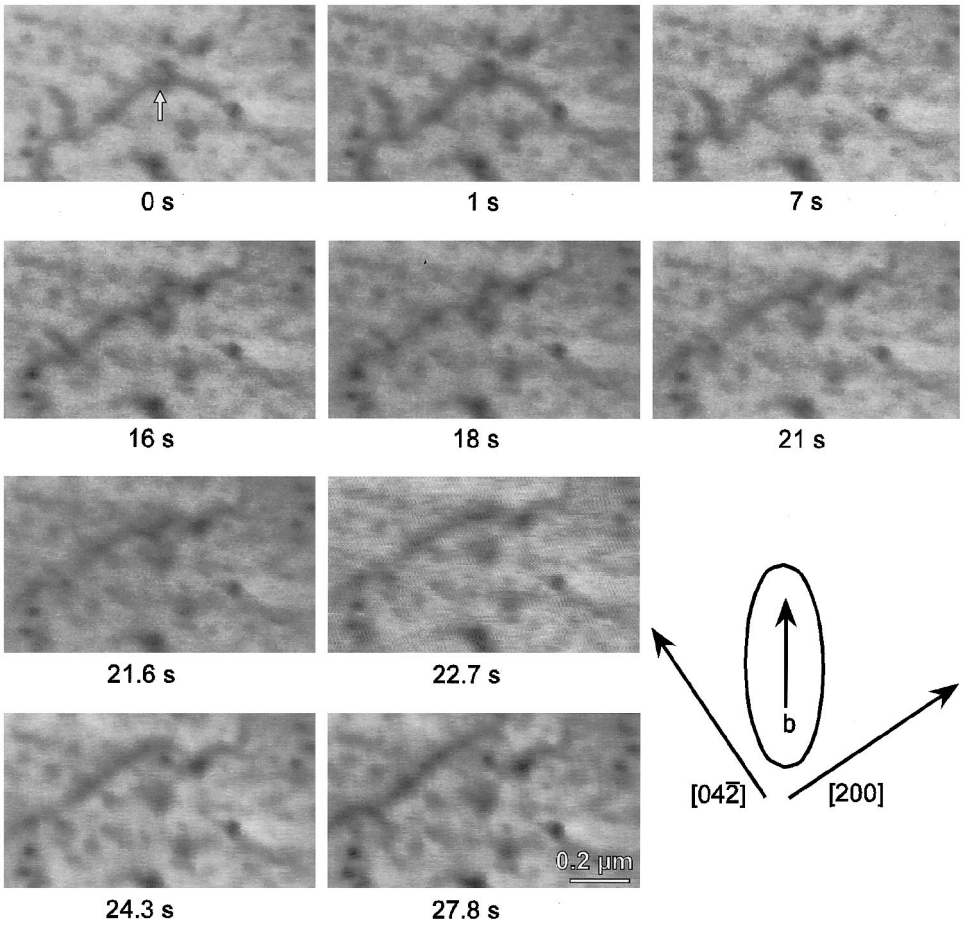

Fig. 3. Video sequence of a dislocation moving at 700°C on a {112} plane inclined by about 25° with respect to the image plane.

anisotropic medium [15]. The elastic constants were taken from [16] for the alloy PM 2000, which should be similar to INCOLOY MA 956. As an example, $c_{11} = 140.5$ GPa, $c_{12} = 97$ GPa and $c_{44} = 102.7$ GPa at 700°C. Characteristic is the high ratio of anisotropy, which is $A = 2.96$ at room temperature, and $A = 4.7$ at 700°C. The shape of the loops was calculated for room temperature and 700°C for the {110}, {112} and {123} slip planes observed in this study. Fig. 6 presents the results for 700°C. The ratios between the prelogarithmic terms of the line energies E_e and E_s of edge and screw dislocations of 1.91 at room temperature and of 2.32 at 700°C, listed in Table 1, are reflected in the large values of the ratios between the major and minor half axes of the dislocation loops. The line tension of the dislocations becomes negative at dislocation orientations (angles between dislocation line and Burgers vector) between about 125 and 140° on the (011) slip plane, between 85 and 95° on the (112) plane, and between 45 and 55°, as well as at 95°, on the (123) plane. A high value of the line tension of screw dislocations and their resulting low curvature are responsible for the fact that the bowed-out segments could not be identified along the screw dislocations at room temperature.

The calculated loops were plotted with different sizes in the projection of the electron micrographs for Burgers vector directions with a sufficiently high orientation factor. Usually, Burgers vectors could be assigned unequivocally to the dislocations with bowed-out segments because of the strong ellipticity of the calculated loops. Examples of single loops are given in Figs. 1–3 in a size larger than that fitting to the bowed-out segments. Loops of an appropriate size were selected to fit the experimental shapes of bowed-out dislocation segments as described in [17]. The lengths of the minor half axes y_o of the fitting loops, as marked in Fig. 6, were used to describe the curvature of the individual segments. The y_o values are related to the back (shear) stresses τ_b acting on the individual segments by

$$\tau_b = [E_s/(by_o)] \ln\{l/(\beta r_o)\} \quad (1)$$

Here, E_s is the prelogarithmic term of the energy of a screw dislocation as above. b is the absolute value of the Burgers vector, and r_o the inner cut-off radius, which is set $r_o = b$. β is a numerical constant equal to 5, which considers the mutual interaction between the bowed-out segments ([18], see also Ref. [19]). At 700°C, the obstacle distances l are measured on the individual

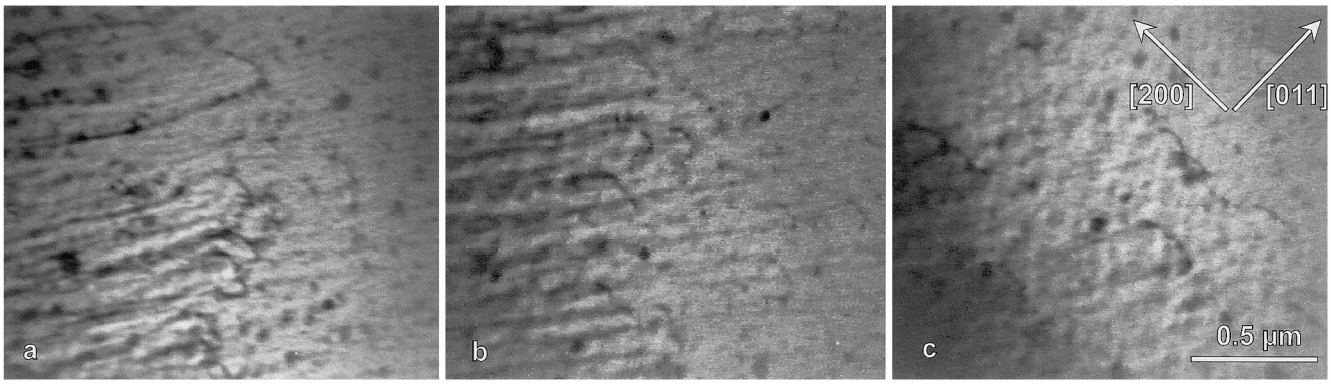

Fig. 4. Video frames of dislocation configurations recorded during in situ deformation of a single specimen of MA956 at temperatures of (a) 660, (b) 880 and (c) 1010°C. Slip observed mainly on {011} planes.

bowed-out segments. For room temperature, an average distance of 141 nm of bowed-out segments was used, as discussed above. Average values of the observed back stresses τ_b are listed in Table 1.

To characterize the dynamic behaviour of dislocations at high temperatures, the displacement s of the dislocations was plotted versus the time t. Fig. 7 shows an example, with four curves originating from different positions along the single dislocation presented in Fig. 3. Other moving dislocations show a similar behaviour. This plot demonstrates that only parts of the dislocations are pinned temporarily while others still move, leading to a relatively homogeneous motion of the dislocations as a whole, and that the times of resting and moving are of the same order of magnitude as concluded qualitatively already in Section 3.2.

3.4. Results of macroscopic deformation tests

Two samples were tested at a basic strain rate of 10^{-4} s^{-1}, one at room temperature up to 600°C, and the second between 600 and 900°C. They show a weak work hardening, most pronounced at 300°C, and yield drop effects at 600 and 700°C. Fig. 8 presents the dependence of the flow stress σ on the temperature. From the measured critical flow stresses at the individual temperatures, the stress increments due to work hardening of the preceding strainings were subtracted so that the data should correspond to the critical flow stresses at the respective temperatures. The flow stresses show an initial decrease above room temperature, perhaps a plateau at 300–400°C, and again a decrease at higher temperatures.

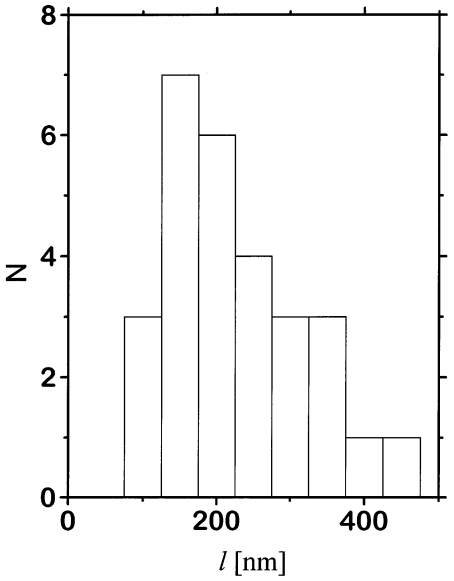

Fig. 5. Histogram of obstacle distances measured along a single dislocation during 3 min observation of the video tape recording presented in Fig. 3. N is the number of measurements.

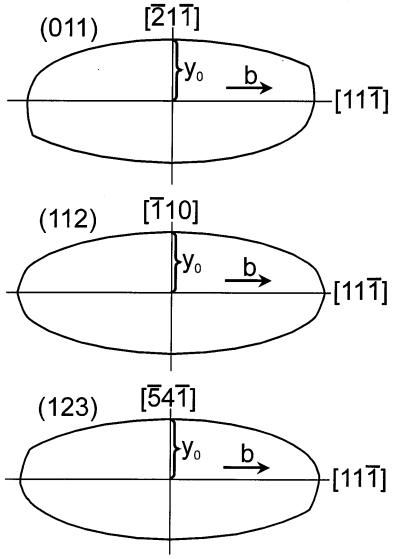

Fig. 6. Theoretical shape of dislocations under stress on (011), (112) and (123) planes. Calculations based on the line tension model for an elastically anisotropic medium, using the elastic constants of the alloy PM 2000 at 700°C [16].

Table 1
Average values of the obstacle distances l, the minor axis y_o of fitting calculated dislocation loops, resulting back stresses τ_b, prelogarithmic terms of the energy factors of screw and edge dislocations (on {110} planes), E_s and E_e, and the Orowan stresses $\tau_{OR\,s}$ and $\tau_{OR\,e}$ at different temperatures T

T (°C)	l (nm)	y_o (nm)	τ_b (MPa)	E_s (N)	E_e (N)	$\tau_{OR\,s}$ (MPa)	$\tau_{OR\,e}$ (MPa)
23	141[a]	111	56	2.91×10^{-10}	5.57×10^{-10}	182	95
700	200	141	25	1.72×10^{-10}	4×10^{-10}	131	56
880				1.46×10^{-10}	3.55×10^{-10}	116	48

[a] This value corresponds to the dislocation segments used for measuring the dislocation curvature. It is not characteristic of all segments.

Some typical stress relaxation curves are plotted in Fig. 9 as $\ln(-\dot{\sigma})$ versus σ, where the strain rate sensitivity of the stress r corresponds to the reciprocal slope of these curves. At room temperature, the curves are straight, indicating that the strain rate sensitivity does not depend on the relaxation rate itself, which is proportional to the strain rate. At 300°C, the relaxation curve is very steep. At high temperatures, for instance at about 700°C, the curves show a 'usual' curvature with a decreasing strain rate sensitivity for a decreasing strain rate or stress. However, at intermediate temperatures as, for instance at 500°C, the curves exhibit a steep part at the beginning, leading to an 'inverse' curvature. Fig. 10 shows the strain rate sensitivity r as a function of temperature. Data points with full symbols are calculated from the slope at the beginning of the relaxation tests (e.g. dashed line along the curve for 500°C in Fig. 9). Accordingly, they correspond to the strain rate of the continuous deformation before the relaxation tests. In the cases of an 'inverse' curvature of the relaxation curves, r values are determined also for the range of intermediate relaxation rates (dotted line in Fig. 9). In Fig. 10, these values are plotted as open symbols. This figure shows that the strain rate sensitivity decreases from about 5.5 MPa at room temperature down to 1.2 MPa at 300°C. Afterwards, the initial values exhibit a maximum at about 600°C and decrease again above 700°C, down to a very small value at 900°C. The strain rate sensitivity at intermediate relaxation rates (open symbols) shows a strong maximum at about 500°C. The few strain rate cycling tests performed confirm the results of the stress relaxation tests. Below, the strain rate sensitivity will be discussed also in terms of the stress exponent $m = \mathrm{d}\ln\dot{\varepsilon}/\mathrm{d}\ln\sigma = \sigma/r$. The temperature dependence of m is plotted in Fig. 11.

4. Discussion

In the following, processes will be discussed which may control the flow stress of the alloy INCOLOY MA956 at different temperatures. The temperature dependence of the flow stress presented in Fig. 8 is qualitatively very similar to that measured on the similar alloy PM 2000 [20–22]. However, the present values are lower and they are also lower than those measured previously on MA 956 (e.g. [23]). This may result from the lower strain rate and the single-crystal character of the small specimens in the present study.

4.1. Long-range dislocation interactions

Mutual elastic interactions between dislocations may contribute to the flow stress by the so-called Taylor hardening [24]. The respective contribution to the shear stress is given by

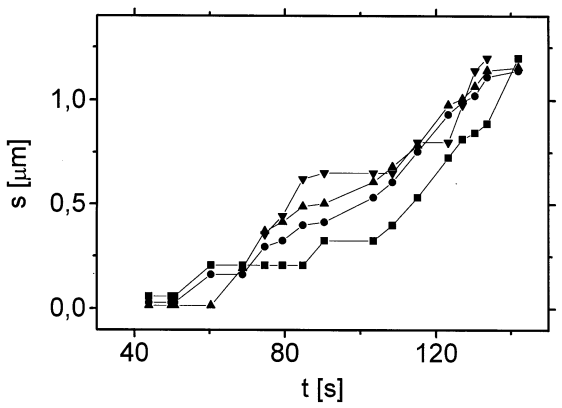

Fig. 7. Plots of dislocation displacement s versus time t at 700°C. The four curves correspond to different points marked along the single dislocation line presented in Fig. 3.

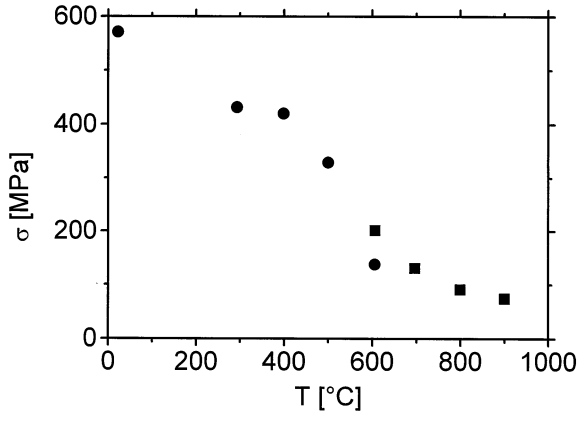

Fig. 8. Temperature dependence of the critical flow stress σ. Data from two samples (squares and circles). For correction of work hardening see text.

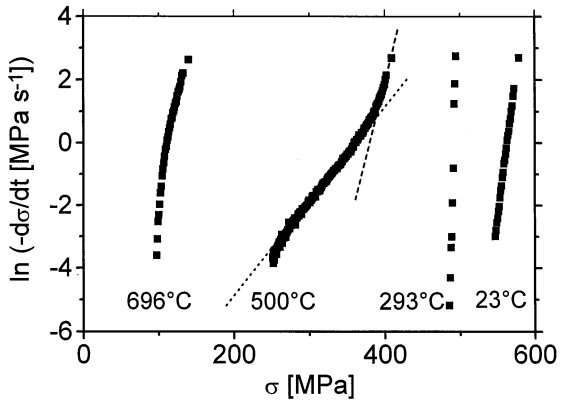

Fig. 9. Typical stress relaxation curves obtained for temperatures between 23 and 693°C.

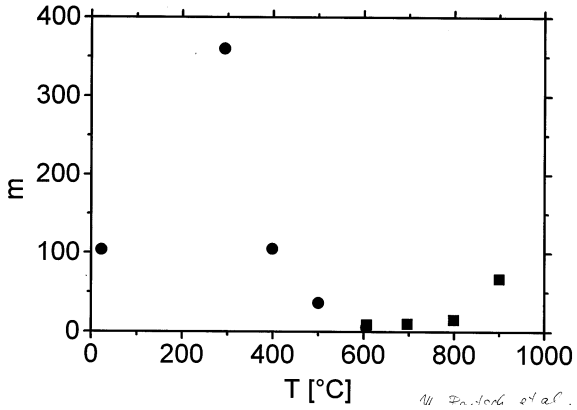

Fig. 11. Temperature dependence of the stress exponent m of the strain rate.

$$\tau_i = \alpha\mu b\rho^{1/2} \quad (2)$$

where α is a numerical factor, μ is the shear modulus, and ρ is the dislocation density. For a rough estimate, α is chosen equal to 0.5 and $\mu = 4\pi E_s/b^2$. This yields $\mu \cong 60$ GPa at room temperature, and 30 GPa at 880°C. Dislocation density data of deformed specimens are rare and slightly controversial [25,26]. The dislocation density seems to be constant between 400 and 600°C at $\rho \cong 5 \times 10^{13}$ m^{-2} yielding $\tau_i \cong 40$ MPa at some intermediate temperature. At high temperatures, ρ decreases down to 2.5×10^{13} m^{-2} [25]. At 400°C, deformation is localized in shear bands having a very high dislocation density of 3.5×10^{15} m^{-2} [26]. This yields the very high internal stress contribution of $\tau_i \cong 300$ MPa. To compare the calculated stresses with macroscopic flow stress data, the relation $\tau = m_s\sigma$ between the shear stress τ and the compressive stress σ has to be considered. m_s is the orientation factor, which may be set equal to 0.4 for the single-crystal like macroscopic specimens. It may therefore be concluded that Taylor hardening contributes essentially to the critical flow stress of MA956 at all temperatures. Unfortunately, no dislocation density data are available for room temperature.

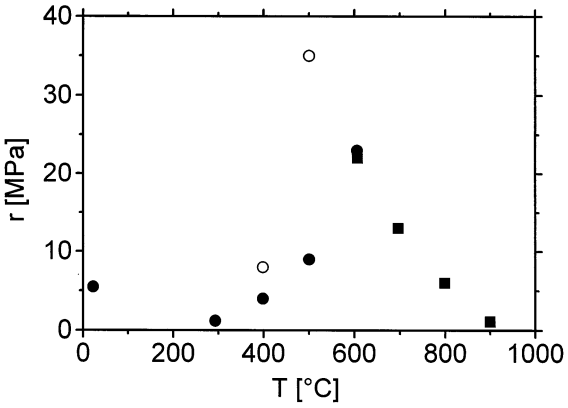

Fig. 10. Temperature dependence of the strain rate sensitivity of stress r. Values of r taken at the beginning of the relaxation tests (corresponding, e.g. to the dashed line along the relaxation curve for 500°C in Fig. 9) are shown with full symbols, and those determined at intermediate relaxation rates (like the dotted line in Fig. 9) with open symbols. Squares and circles correspond to different samples.

4.2. Orowan stress

The array of oxide particles can be characterized by an average particle diameter of $d = 24$ nm and a volume fraction of $f = 0.0145$ [12,26]. The volume fraction was estimated from the distribution of the diameters and the total density of the particles via a stereological formula. From these data, the average obstacle distance l on the slip plane can be calculated in the most simple way (see, e.g. Ref. [27]) according to

$$l = d(\pi/6f)^{1/2} \quad (3)$$

which yields $l \cong 150$ nm. At zero temperature, these obstacles can be bypassed only if the applied shear stress exceeds the Orowan stress, given in Ref. [28]

$$\tau_{OR} = [2E/\{b(l-d)\}]\{\ln(X/b) + 0.7\} \quad (4)$$

Here, for the Orowan stress of screw or edge dislocations, E is the prelogarithmic factor of the line energy of edge or screw dislocations. For small particles, the length parameter

$$X = d(1 - d/l) \quad (5)$$

is almost equal to the diameter d. Eq. (4) and Eq. (5) consider the elastic interaction between the dislocation branches attached to the particles but not the random arrangement of the latter. Calculated Orowan stresses, based on the data of d and l quoted above, are listed in Table 1. Considering the random arrangement of the particles would reduce the Orowan stresses by about 20%. There is a great difference between the theoretical values of the Orowan stresses of screw and edge dislocations. However, there was no indication in the in situ experiments that the particles are overcome preferentially by edge dislocation segments. If the orientation

factor is considered, the average values of the Orowan stress σ_{OR} for screw and edge dislocations amount to about 350 MPa at room temperature, and to 200 MPa at 880°C. These values should be considered the upper limits.

The obstacle distance of about 200 nm observed in the in situ experiments at 700°C is slightly larger than the value of 150 nm calculated by Eq. (3) based on the particle diameter and the volume fraction. This may imply that only a fraction of the particles, probably the larger ones, impede the dislocation motion effectively. Considering this and taking into account a factor of 0.84 for the random arrangement of the particles [28], the values of the Orowan stress become about 40% less, i.e. they are $\sigma_i \cong 210$ MPa at room temperature, and 120 MPa at 880°C.

Both long-range dislocation interactions and the Orowan stress are of athermal character. It is therefore proposed that the flow stress plateau between about 300 and 400°C in Fig. 8 is controlled by these two mechanisms. In this case, the back stress τ_b estimated in Section 3.3. should approximately be equal to the Orowan stress. The value of the back stress at room temperature in Table 1 of $\tau_b = 56$ MPa was measured along edge dislocations. It fits the discussed range of Orowan stresses for edge dislocations of $\tau_{OR\,e} = 95$ MPa–40%, but not the average Orowan stress $\tau_{OR} \cong 140$ MPa–40%. This discrepancy may illustrate the accuracy (or the errors) of the experimental and theoretical methods used. As demonstrated in Fig. 10, the strain rate sensitivity is very low at 300°C in agreement with the athermal character of the deformation in this temperature range. The drastic decrease of the flow stress above 400°C should then be due to the thermally activated overcoming of the oxide particles but also to a decreasing contribution of Taylor hardening due to recovery. This view is supported by the fact that the particle-free matrix material Kanthal shows the same plateau as well as the decrease of the flow stress above 400°C [22]. Both processes leading to the flow stress decrease require diffusion. Above about 500°C, the flow stress should be lower than the Orowan stress. This is indicated in Table 1 where the back stress τ_b at 700°C is only 27% of the average Orowan stress.

4.3. The thermally activated detachment model

As discussed already, above about 500°C the flow stress of the alloy MA956 is lower than the Orowan stress. Only in this case, the theory of Arzt and Rösler [1–6] can be applied. This theory assumes that after overcoming the particles by climb, the dislocations become pinned at their departure side. In the athermal case, the stress for the detachment of the dislocations from the particles is given by

$$\tau_d = \tau_{OR}(1-\kappa^2)^{1/2} \quad (6)$$

κ is a parameter describing the relaxation of the stress field of the dislocation at the particle surface. Eq. (6) is refined in Ref. [29] by considering the dispersoids as weak obstacles in a random arrangement. Nevertheless, the present qualitative discussion is based on the simple Eq. (6). At a finite temperature, the dislocations can detach from the particles at stresses lower than τ_d. They spend most of their time at the departure side of the particles waiting for the thermally activated detachment so that this process controls the average dislocation velocity. The in situ experiments described in Section 3.2 and Section 3.3 show clearly that this does not happen at 700°C. Fig. 7 demonstrates that mostly only parts of a dislocation are resting while others are still moving, and that the travelling times between the stable positions are approximately equal or even longer than the lifetimes in the pinned positions. As discussed in connection with Fig. 3, the dislocations spend a long time for bowing between the particles before they reach their elastic equilibrium positions. The time of waiting for detachment is only a small fraction of the total time. However, frictional forces must impede the dislocation motion and result in their viscous motion, which will be discussed below. No frictional stress is considered in the thermally activated detachment model.

As pointed out in Section 3.2 in connection with Fig. 4, above 700°C the dislocation motion becomes jerky indicating that the frictional stress is no longer important while the dislocations are still pinned to the particles. This can be explained by the Orowan process still active at high temperatures but it is also consistent with the thermally activated detachment model.

For the Orowan process, the temperature dependence of the flow stress is only due to the temperature dependence of the energy factor E of the dislocations in Eq. (4). Respective values of the Orowan stress are listed in Table 1 for screw and edge dislocations at different temperatures. Accordingly, the temperature sensitivity of the stress contribution of the Orowan process amounts to $d\sigma_{OR}/dT \cong -0.21$ MPa K^{-1} for screw dislocations, and to about -0.11 MPa K^{-1} for edge ones at temperatures above 700°C. The experimental value is $d\sigma/dT \cong -0.4$ MPa K^{-1} between 700 and 800°C. Thus, the flow stress above 700°C depends on the temperature more strongly than predicted by the Orowan mechanism. The reason is the operation of a thermally activated mechanism, for instance the thermally activated detachment model.

According to Ref. [6], in this model the stress exponent can be expressed by

$$m = [3\Gamma d/(2kT)](1-\kappa)^{3/2}(1-\tau/\tau_d)^{1/2}\tau/\tau_d \quad (7)$$

Γ is the line tension and kT are Boltzmann's constant and temperture. For a rough estimate, an average value

of $E \cong 3 \times 10^{-10}$ N can be used for Γ. κ is not known very well. According to Ref. [30], $\kappa = 0.66$ for PM 2000. The terms $(1-\tau/\tau_d)^{1/2}$ τ/τ_d depend on τ/τ_d only weakly. The stress acting locally is given by the back stress τ_b. With the data listed in Table 1 for 700°C, $\tau_b/\tau_{OR} \cong 0.27$ or, with Eq. (6), $\tau/\tau_d \cong 0.3$. With these data, the theoretical value of m turns out to be about 40 at this temperature and to decrease with increasing temperature. The experimental values of m in Fig. 11 increase from about 10 at 700°C up to about 70 at 900°C. While the experimental values of the stress exponent are in the correct order of magnitude of the estimated one, their temperature dependence contradicts the theoretical dependence of the thermally activated detachment model so that the deformation between about 700 and 900°C should not be controlled by this model. Above 900°C, m is reported to decrease [30] so that the model may be active in this high-temperature range. However, the high values of m at high temperatures may also hint to an increasingly athermal character of the deformation, which should be controlled mainly by τ_i.

4.4. Solution hardening

As noted in Section 2, the studied alloy INCOLOY MA956 consists (in wt%) of Fe–19.9Cr–4.6Al–0.38Ti–0.51Y–0.019C–0.014N–0.19O. The Ti and perhaps also a fraction of the Al atoms as well as the C and N impurities may give rise to solution hardening. Solution hardening is understood here as the interaction between dislocations and non-diffusing solutes. The order of magnitude of the parelastic interaction energy between the solutes and the dislocations can be estimated roughly by

$$\Delta G_o \cong \mu b^3 \delta \quad (8)$$

where δ is the size misfit (see, e.g. Ref. [31]). Using $\mu \cong 60$ GPa as in Section 4.1 and a (usual) value of $\delta = 0.1$ yields $\Delta G_o \cong 0.6$ eV. Such weak obstacles can give rise to the low-temperature increase of the flow stress of about 150 MPa between 300°C and room temperature in Fig. 8, and to the simultaneous increase of the strain rate sensitivity in Fig. 10. However, they are easily overcome at high temperatures.

From the strain rate sensitivity r, an activation volume V can be calculated according to

$$V = kT/(m_s r) \quad (9)$$

As above, m_s is the orientation factor. At room temperature with $r = 5.5$ MPa, V amounts to about $120b^3$. The obstacle distance l_s between the solutes can roughly be estimated by $l_s \cong b/c^{1/2}$, where c is the atomic concentration. With c being a fraction of a percent, l_s will be of the order of magnitude of $15b$. If the solutes are overcome individually, l_s is related to V by $V = l_s b \Delta$, where Δ is the so-called activation distance. For solutes, $\Delta \cong b$ so that the measured activation volume is about one order of magnitude larger than that concluded from the solute concentration. This discrepancy can be explained by the statistical theory of solution hardening [32], which considers that the solutes are not overcome individually but in a collective way. Thus, a small part of the flow stress near room temperature can consistently be explained by solution hardening. It follows from the jerky motion of dislocations at room temperature that this part is only small. In particular, solution hardening will not be responsible for the high-temperature friction mechanism causing the viscous dislocation motion observed in the in situ experiments at 700°C.

4.5. Diffusional point defect drag

At high temperatures, the solutes may diffuse giving rise to a dynamic point defect drag. The physical origins and the respective theories are described in Ref. [33]. It is suggested here that the point defect drag controls the velocity of the viscously moving dislocations in the temperature range around 700°C, described in Section 3.2 and Section 3.3. It is estimated in Ref. [34] for a similar situation and experimentally proved on different materials as reviewed in Ref. [35] that some 1000 ppm of a solute are necessary for a remarkable contribution to the flow stress. Such a concentration should be available in the alloy investigated.

As pointed out in Refs. [34,36], point defect drag may cause an inverse dependence of the strain rate sensitivity on the strain rate, i.e. a decreasing strain rate sensitivity with increasing strain rate or stress. This is observed here as an inverse curvature of the stress relaxation curves at 400 and 500°C, as described in Section 3.4 and shown in Fig. 9 for the curve at 500°C. Accordingly, the point defect drag may cause the whole maximum of the strain rate sensitivity in Fig. 10 between about 300 and 800°C, as well as a contribution to the flow stress, showing a maximum, too. This process is superimposed on a very rapid high-temperature decrease of the flow stress above 400°C. Nevertheless, the dynamic point defect drag should be responsible for the viscous motion of dislocations observed in the in situ experiments around 700°C. Thus, this mechanism should represent the thermally activated process during the high-temperature deformation of MA956 up to 900°C. The travelling times in an ODS material have been considered before in the composite model described in Refs. [8,30].

5. Conclusions

In situ straining experiments in an HVEM on the ferritic oxide dispersion strengthened alloy INCOLOY

MA956 allowed the direct observation of the dislocation motion through an array of oxide particles at room temperature and between 640 and 1010°C. The description of the dislocation dynamics supported by macroscopic compression tests including stress relaxation experiments lead to the following conclusions.

1. At room temperature and at temperatures up to 1010°C, dislocations bow out under load between the oxide particles. Between the particles they move jerkily at room temperature and above about 750°C, but viscously in a certain range below that temperature.
2. At temperatures below 400°C, both long-range dislocation interactions and the Orowan stress of the oxide particles yield the main contributions to the flow stress.
3. A diffusional point defect drag may result in the viscous dislocation motion between particles at intermediate temperatures, in a maximum of the strain rate sensitivity between 300 and 800°C and in a contribution to the flow stress in this temperature range. While the dislocations are pinned at the departure side of the oxide particles, there is no indication that the thermally activated detachment from these positions controls the deformation around 700°C.
4. In this range, the main effect of the particles seems to be the temporary reduction of the velocity of viscous glide owing to the back stress of the dislocation segments bowing out between the particles.
5. Above 900°C, the thermally activated detachment model and long-range interactions between dislocations may be the important deformation mechanisms.
6. Solution hardening may give rise to the low-temperature increase of the flow stress near room temperature.

Further experiments are necessary to identify the processes controlling the flow stress of the ODS alloy INCOLOY MA956 in more detail.

Acknowledgements

The authors are grateful to Dr Dietmar Baither for making available his PC programme for calculating the dislocation line energy and line tension data in anisotropic elastic media as well as to Bert Geyer and Clemens Ladisch for their programme for simulating the geometry of slip trails. The authors thank Christian Dietzsch and Wolfgang Greie for their technical assistance. Two of them (A.W. and A.C-F.) acknowledge financial support of the University of Mining and Metallurgy (Grant Nr. 10.10.110.31).

References

[1] J. Rösler, E. Arzt, Acta Metall. 36 (1988) 1043.
[2] E. Arzt, D.S. Wilkinson, Acta Metall. 34 (1986) 1893.
[3] D.J. Srolovitz, R. Petkovic-Luton, M.J. Luton, Scripta Metall. 16 (1982) 1401.
[4] D.J. Srolovitz, M.J. Luton, R. Petkovic-Luton, D.M. Barnett, W.D. Nix, Acta Metall. 32 (1984) 1079.
[5] E. Arzt, J. Rösler, Acta Metall. 36 (1988) 1053.
[6] J. Rösler, E. Arzt, Acta Metall. 38 (1990) 671.
[7] J.H. Schroeder, E. Arzt, Scripta Metall. 19 (1985) 1129.
[8] R. Herzog, A. Wasilkowska, A. Czyrska-Filemonowicz, H. Schuster, in: IXth Conf. on Electron Microscopy of Solids, Kraków-Zakopane, 1996, p. 379.
[9] R. Behr, J. Mayer, E. Arzt, Intermetallics 7 (1999) 423.
[10] H. Schuster, R. Herzog, A. Czyrska-Filemonowicz, Metall. Foundry Eng. 21 (1995) 273.
[11] B. Dubiel, M. Wróbel, P.J. Ennis, A. Czyrska-Filemonowicz, Scripta Mater. 37 (1997) 1215.
[12] A. Wasilkowska, M. Bartsch, U. Messerschmidt, A. Czyrska-Filemonowicz, in: J. Kusinski, I. Suliga, S. Kac (Eds.), Proc. XV Conf. on Advanced Materials and Technologies, Krakow-Krynica 1998, Inzyniera Materialowa No. 3 (1998) 463.
[13] U. Messerschmidt, F. Appel, Ultramicroscopy 1 (1976) 223.
[14] U. Messerschmidt, M. Bartsch, Ultramicroscopy 56 (1994) 163.
[15] G. DeWitt, J.S. Koehler, Phys. Rev. 116 (1959) 1113.
[16] W. Hermann, Ph.D. Thesis, University of Erlangen-Nürnberg, 1995.
[17] U. Messerschmidt, Z. Metallkd. 84 (1993) 391.
[18] R.O. Scattergood, D.J. Bacon, Phil. Mag. 31 (1975) 179.
[19] U. Messerschmidt, F. Appel, H. Schmid, Phil. Mag. A 51 (1985) 781.
[20] J.H. Lee, Ph.D. Thesis, University of Erlangen-Nürnberg, 1994
[21] J. Wunder, Ph.D. Thesis, University of Erlangen-Nürnberg, 1997, Fortschr.-Ber. VDI, Reihe 5, No. 510, Düsseldorf 1997.
[22] B. Reppich, M. Heilmaier, J. Wunder, H. Baumeister, T. Huber, in: H. Mughrabi, G. Gottstein, H. Mecking, H. Riedel, J. Tobolski (Eds.), Microstructure and Mechanical Properties of Metallic High-Temperature Materials, Wiley-VCH, Weinheim, New York, 1999, p. 509.
[23] B. Dubiel, W. Osuch, M. Wróbel, P.J. Ennis, A. Czyrska-Filemonowicz, J. Mater. Proc. Technol. 53 (1995) 121.
[24] G.J. Taylor, Proc. R. Soc. London A145 (1934) 362.
[25] A. Wasilkowska, Ph.D Thesis, University of Mining and Metallurgy, Kraków, 1998.
[26] A. Czyrska-Filemonowicz, B. Dubiel, J. Mater. Proc. Technol. 64 (1997) 53.
[27] A.J. Ardell, Metall. Trans. A 16 (1985) 2131.
[28] D.J. Bacon, U.F. Kocks, R.O. Scattergood, Phil. Mag. 26 (1973) 1241.
[29] B. Reppich, Acta Mater. 46 (1998) 61.
[30] R. Herzog, Ph.D. Thesis, RWTH Aachen, 1997.
[31] P. Haasen, in: F.R.N. Nabarro (Ed.), Dislocations in Solids, vol. 4, North-Holland, Amsterdam, 1997, p. 155.
[32] R. Labusch, R. Schwarz, in: D.G. Brandon, R. Chaim, A. Rosen (Eds.), Strength of Metals and Alloys, Freund, London, 1991, p. 47.
[33] J.P. Hirth, J. Lothe, Theory of Dislocations, Wiley-Interscience, New York, 1982.
[34] U. Messerschmidt, M. Bartsch, S. Guder, D. Häussler, Proc. Mater. Res. Soc. 552 (1999) p. kk10.9.1.
[35] L.P. Kubin, Y. Estrin, J. Phys. Paris III 1 (1991) 929.
[36] U. Messerschmidt, M. Bartsch, S. Guder, D. Häußler, R. Haushälter, M. Yamaguchi, Intermetallics 6 (1998) 729.